



**ARTICLE**

# Mechanical Test and Meso-Model Numerical Study of Composite Rubber Concrete under Salt-Freezing Cycle

Mingkai Sun<sup>1,\*</sup>, Yanan Wang<sup>2</sup>, Pingwei Jiang<sup>1</sup>, Zerong Song<sup>3</sup>, Zhan Gao<sup>4</sup> and Jiaming Xu<sup>5</sup>

<sup>1</sup>Key Laboratory of Urban Security and Disaster Engineering of Ministry of Education, Beijing University of Technology, Beijing, 100124, China

<sup>2</sup>Powerchina Eco-Environmental Group Co., Ltd., Shenzhen, 518000, China

<sup>3</sup>School of Civil Engineering and Communication, North China University of Water Resources and Electric Power, Zhengzhou, 450003, China

<sup>4</sup>Shenzhen Gas Corporation, Ltd., Shenzhen, 518049, China

<sup>5</sup>The Second Engineering Co., Ltd. of CTCE Group, Suzhou, 215000, China

\*Corresponding Author: Mingkai Sun. Email: Mingkai2020@emails.bjut.edu.cn

Received: 24 February 2022 Accepted: 13 May 2022

## ABSTRACT

A composite rubber concrete (CRC) was designed by combining waste tire rubber particles with particle sizes of 3~5 mm, 1~3 mm and 20 mesh. Taking the rubber content of different particle sizes as the influencing factors, the range and variance analysis of the mechanical and impermeability properties of CRC was carried out by orthogonal test. Through analysis, it is concluded that the optimal proportion of 3~5 mm, 1~3 mm, and 20 mesh particle size composite rubber is 1:2.5:5. 5 kinds of CRC and 3 kinds of ordinary single-mixed rubber concrete (RC) with a total content of 10%~20% were designed under this ratio, and the salt-freezing cycle test was carried out with a concentration of 5% Na<sub>2</sub>SO<sub>4</sub> solution. The physical and mechanical damage laws during 120 salt-freezing cycles are obtained, and the corresponding damage prediction model is established according to the experimental data. The results show that: on the one hand, the composite rubber in CRC produces a more uniform “graded” structure, forms a retractable particle group, and reduces the loss of mechanical properties of CRC. On the other hand, colloidal particles with different particle sizes are used as air entraining agent to improve the pore structure of concrete and introduce evenly dispersed bubbles, which fundamentally improves the durability of concrete. Under the experimental conditions, the CRC performance is the best when the overall content of composite rubber is 15%.

## KEYWORDS

Waste rubber; composite rubber concrete; orthogonal test; mechanical properties; durability

## 1 Introduction

With the ever-expanding working population, the global demand for automobiles has increased significantly, so the number of end-of-life car tires is increasing every year. Due to the non-biodegradability of rubber tires, the main treatment methods for waste rubber tires at present are landfill, reuse or disposal as combustion materials [1–3]. However, these methods will inevitably have an impact on the ecological environment such as groundwater, formation soil, and atmosphere. Therefore, the



management of scrap tires has become a growing problem [4–6]. It is estimated that by the end of 2030, the world will generate 1.2 billion scrap tires annually [7]. In recent years, the use of waste rubber tire particles to replace natural concrete aggregates in concrete and asphalt mixtures to make rubber concrete. Due to the excellent properties of rubber concrete such as light weight, high toughness, and high damping [8,9], the use of waste rubber tires to prepare concrete mixtures in the construction industry is a sustainable solution.

At present, in terms of macroscopic experiments, many scholars have conducted various studies to enhance the performance of rubberized concrete by considering (a) the size of the rubber particles (b) the amount of rubber (c) the effect of the treatment type of the rubber particles [10–12]. Toutanji [13] explored the method of replacing fine aggregates with rubber particles of different particle sizes (1, 3, 5 mm). The results showed that the larger the rubber particles, the more obvious the decrease in concrete strength. Tantala et al. [14] studied the compressive strength of concrete made with 1–3 mm rubber particles instead of fine aggregates, and found that the compressive strength of concrete was better when rubber particles replaced 10% of fine aggregates. Osama et al. [15] studied rubberized concrete with different rubber particle sizes (0.15–2.36 mm) and grades of 20, 25, and 32 MPa, respectively. The performance was compared with ordinary concrete after standard curing. The results show that in the range of rubber particle size (0.15–2.36 mm), the increase of rubber particle size reduces the loss of compressive strength of rubber. Compared with ordinary concrete, replacing sand with 20% rubber can reduce the 7-day/28-day strength ratio by 9% to 20%. Xu et al. [16] mainly analyzed the mechanical properties and acoustic emission (AE) parameters under biaxial compression stress states of CRC with different rubber contents (0%, 5% and 10%). The experiment results showed that the compressive strength and peak strain of CRC are improved under biaxial stress like plain concrete (PC), but due to the weak bond between rubber and cement-based materials, the strength. Al-Tayeb et al. [17] studied the effect of different contents of 20 mesh and 1–3 mm rubber particles on the fracture properties of concrete. Studies have shown that 20 mesh rubber particles are better than 1–3 mm rubber particles for the improvement of fracture properties. Zhang et al. [18] used ultrasonic technology to explore the damage process of rubber concrete under three-point bending. The experimental results show that the rubberized concrete exhibits a smaller damage area than the ordinary concrete. Ali et al. [19] studied the effect of 4 mm rubber particles on the fracture parameters and cracking properties of rubber concrete under different contents. The results show that with the increase of rubber content, the ductility of rubber increases gradually, and the load-displacement curve tends to be flat. Xu et al. [20] analyzed the mechanical properties and acoustic emission parameters of RCs with different rubber contents (0%, 5%, 10%) under bidirectional compressive stress using rubber particles with a particle size of 1.13–2.55 mm. The test results show that the compressive strength and peak strain of RC are improved under the action of bidirectional stress, but its strength growth rate is lower than that of ordinary concrete due to the weak adhesion between rubber and cement-based materials. The above macroscopic experiments are all studies on the mechanical and other properties of concrete with different particle sizes and different dosages. Most of the experiments can only reflect the influence of rubber particles on various properties of concrete based on experimental data, but cannot explain the fundamental reasons for the large differences in the mechanical properties of various rubber concretes from a microscopic point of view. Therefore, some scholars have studied the mesoscopic model of rubber concrete. Chen et al. [21] used Python program and Abaqus to simulate the compressive strength of rubber concrete with different rubber contents, shapes and sizes. Numerical results confirm that the stiffness of rubber concrete is reduced compared to that of ordinary concrete. The rubber content and the shape of the rubber particles are the main factors that reduce the Young's modulus. The compressive strength of the rubber concrete is better when the rubber content is 10%–12%. Based on the cohesive crack model, Guo et al. [22] studied the whole process of axial compression failure of rubber concrete with different particle sizes and contents of 1–5 mm using different damage constitutive. The numerical results show that the damage constitutive based on the quadratic stress criterion can better reflect the whole process of the crack initiation to

penetration of the rubber concrete, and the rubber concrete exhibits an obvious plastic failure form when it is damaged by axial compression. Zhou et al. [23] used a rate-dependent viscous crack model to simulate the dynamic tensile behavior of rubberized concrete with different rubber contents. The results show that the dynamic tensile properties of rubber concrete are greatly affected by the rubber content and the interface transition zone. However, the above mesoscopic model of rubber concrete cannot accurately simulate the contact between the concrete matrix and the rubber particles in the actual situation, which makes the results of the mesoscopic model have certain errors. Therefore, it is necessary to further improve the damage constitutive model of the meso-simulation through the experimental data obtained from the macro-experiment.

In view of this, many scholars have carried out macroscopic experiments or mesoscopic simulation analysis of different rubber contents on a single particle size rubber concrete. There are few studies on composite rubber concrete made of rubber particles with different particle sizes and corresponding contents. Therefore, in this paper, 5 composite rubber concretes were designed by combining waste tire rubber particles with particle sizes of 20 mesh, 1~3 mm and 3~5 mm, and their mechanical properties and sulfate erosion tests were carried out. Furthermore, based on the experimental data and explicit dynamic algorithm, the whole process of the axial compression failure of rubber concrete is simulated by using the cohesion crack model and the damage constitutive of the quadratic stress criterion. Finally, the conclusions drawn from the microscopic simulations further reveal the phenomena of the macroscopic experiments.

## 2 Test

### 2.1 Raw Material

Rubber particles: The rubber processed from waste rubber tires is shown in Fig. 1, and the quality indicators are shown in Table 1.

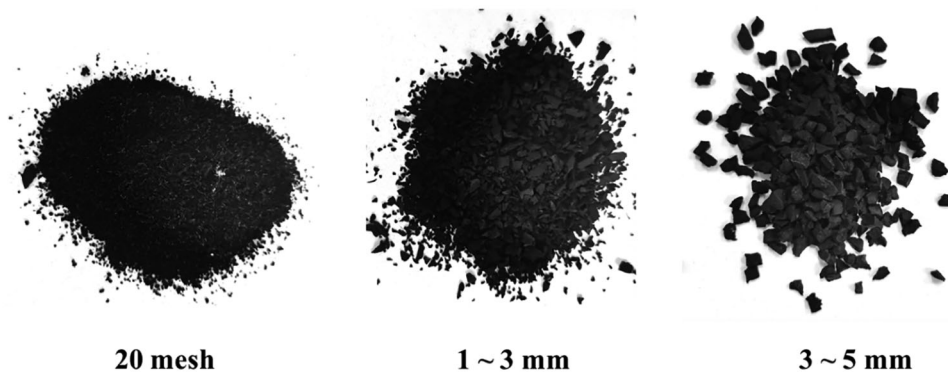


**Figure 1:** Rubber particles with different particle sizes

As can be seen from Fig. 1, the surface of the rubber object is rough and irregular with multiple edges and corners; The microstructure is porous, layered and loose. As an elastomer of flexible material [24], its incorporation into concrete can significantly improve the hard brittleness and corrosion resistance of concrete [20,25,26].

**Table 1:** Rubber particle performance index

Number	Average particle size	Bulk density/kg/m <sup>3</sup>	Apparent density/kg/m <sup>3</sup>	Water content/≤%	Recommended dosage/≤%
1	20 mesh	980	890	0.8	12 [27]
2	1~3 mm	1150	1010	1.3	10 [28]
3	3~5 mm	1210	1090	1.5	5 [28]

Other materials: P·O42.5 composite Portland cement is used for cement. The fly ash is Class I fly ash. Standard medium sand, in which no more than 20% of particles with a particle size of less than 0.075 mm, has a fineness modulus of 2.8. 5~20 mm continuous graded crushed stone. It is mixed with ordinary tap water, and the admixture is HPWR standard high-performance water reducer.

## 2.2 Fabrication of Composite Rubber Specimen

In order to study the effect of the combination of different rubber particles on the performance of concrete, the concrete mix ratio design is carried out according to the concrete design regulations. The mix ratio is cement:sand:stone:water:flyash:admixture = 310:791:1115:150:50:3.4. The mixing ratio of rubber concrete replaces the same volume of medium sand with the combination of rubber particles with different percentages of cementitious material quality. Referring to the recommended dosage of the three rubber particles in Table 1, combine the three rubbers, and use the orthogonal test mix ratio  $L_9 (3^4)$  to analyze the above three-factor and three-level test. The specific mix ratio is shown in Table 2.

**Table 2:** Mix proportions and results of orthogonal experiment

Number	3~5 mm rubber content/%	1~3 mm rubber content/%	20 mesh rubber content/%	Compressive strength/MPa	Flexural strength/MPa	Impermeability/mm
1	1	3	6	28.8	7.3	88.3
2	1	5	8	33.6	8.1	86.1
3	1	7	10	27.5	7.1	83.0
4	2	3	8	32.9	8.2	89.2
5	2	5	10	37.7	8.8	79.8
6	2	7	6	29.6	7.9	92.5
7	3	3	10	29.2	7.5	84.6
8	3	5	6	35.4	8.3	87.5
9	3	7	8	28.7	7.0	91.2

## 2.3 Preparation of Salt Freezing Cycle Test Specimen

In order to explore the influence of the total content of composite rubber on the sulfate resistance of CRC under the condition of the best rubber combination content ratio, the composite rubber with a volume content of 10%~20% was designed to make the corresponding test pieces of wave number, acoustic performance, compressive strength and flexural strength.

## 2.4 Test Method and Equipment

According to the mixing ratio in Tables 2 and 3 test blocks of 100 mm × 100 mm × 100 mm and 6 test blocks of 100 mm × 100 mm × 400 mm were prepared for each group to measure the compressive strength and flexural strength. For each group, 6 circular cone-shaped test blocks with an upper diameter of 175 mm, a lower diameter of 185 mm and a height of 150 mm were prepared to measure the impermeability. Then the test blocks were vibrated and compacted, demolded after 24 h, and placed in an environment with a temperature of  $(20 \pm 2)^\circ\text{C}$  and a relative humidity of over 95% for standard curing for 28 days.

Test CRC strength according to GB/T 50081-2002. The result is calculated according to Eqs. (1) and (2):

$$f_{cc} = 0.95 \times \frac{F}{A_1} \quad (1)$$

$$f_{cf} = 0.85 \times \frac{Fl}{bh^2} \quad (2)$$

where:  $f_{cc}, f_{cf}$  is the compressive strength and flexural strength of CRC, respectively.  $F$  is the failure load of the specimen.  $A_1$  is the bearing area of the test piece and  $l$  is the bearing span.  $b$  is the section width of the test piece.  $h$  is the section height of the test piece. 0.95 and 0.85 are the size conversion factors of non-standard specimens.

**Table 3:** Range analysis of test result

Index	Influence factor	$K_1$	$K_2$	$K_2$ compared to $K_1$ (%)	$K_3$	$K_3$ compared to $K_1$ (%)	$R$	$R^*$ (%)	Factor significance
Compressive strength/MPa	<i>A</i>	29.97	33.40	11.46	31.10	3.78	3.43	31.55	$B > A > C$
	<i>B</i>	30.30	35.57	17.38	28.60	-5.61	6.97	64.12	
	<i>C</i>	31.27	31.73	1.49	31.47	0.64	0.47	4.32	
Flexural strength/MPa	<i>A</i>	7.50	8.20	8.30	7.60	1.33	0.80	39.22	$B > A > C$
	<i>B</i>	7.67	8.40	9.56	7.33	-4.36	1.07	52.45	
	<i>C</i>	7.83	7.77	-0.84	7.80	-0.42	0.17	8.33	
Impermeability/mm	<i>A</i>	85.67	86.67	1.17	87.33	1.94	1.67	12.52	$C > B > A$
	<i>B</i>	87.00	84.00	-3.45	88.67	1.92	4.67	35.01	
	<i>C</i>	89.00	88.67	-0.37	82.00	-7.87	7.00	52.47	

Note:  $R_i^*(\%) = R_i / \sum_{i=A}^D R_i$ .

In the salt freezing cycle test,  $\text{Na}_2\text{SO}_4$  solution with the mass fraction of 5% is used to simulate the sulfate environment. The CRC and RC, after standard curing, are soaked in the sulfate solution at room temperature for 4 days. The freeze-thaw test is carried out according to GB/T 50082-2009. After 30 freeze-thaw cycles each time, the compressive strength and flexural strength of the specimen are tested.

The test used the ultrasonic testing analyzer NM-4B non-metal ultrasonic testing instrument produced by Beijing Cangkerui Company (China) to measure the ultrasonic parameters of the specimen under each salt-freezing cycle times. Each test block was arranged with two relative measuring points to calculate the mean value, and the ultrasonic frequency was 50 kHz, the emission voltage is 500 V, and the sampling period is 0.4  $\mu\text{s}$ . After ultrasonic measurement, the compressive strength and flexural strength were measured by CSS-YAW3000 electro-hydraulic servo pressure testing machine manufactured by Changchun Testing Machine Research Institute Co., Ltd. (China). The water seepage height method was used, and the HP-4.0 concrete impermeability meter was used to measure its impermeability. During the test, the water pressure was kept constant at 12.5 MPa within 24 h, and the pressurization process was 4 min.

### 3 Test Results and Analysis

#### 3.1 Effect of Composite Rubber on Mechanical Properties of CRC

The orthogonal test results are shown in Table 2. In order to investigate the influence of the 3~5 mm rubber content  $V_A/\%$  (factor *A*), the 1~3 mm rubber content  $V_B/\%$  (factor *B*) and 20 mesh rubber content  $V_C/\%$  (factor *C*) in rubber concrete on the physical and mechanical properties of CRC test block, the range analysis and variance analysis of each orthogonal test is carried out.

### 3.1.1 Range Analysis

Through the range analysis, the primary and secondary factors of the test and the optimal combination can be obtained intuitively. Calculated according to Eq. (3), and the analysis results are shown in Table 3.

$$R = \max(\bar{K}_{i1}, \bar{K}_{i2}, \bar{K}_{im}) - \min(\bar{K}_{i1}, \bar{K}_{i2}, \dots, \bar{K}_{im}), (i = A, B, C; m = 1, 2, 3) \quad (3)$$

$K_{im}$  is the sum of the test results corresponding to the level of factor  $m$  in the  $i$ -th column.  $\bar{K}_{im}$  is the average value of  $K_{im}$ , and  $R_i$  is the range of the factor in the  $i$ -th column.  $R_i$  reflects the change range of the test index when the level of the  $i$ -th factor changes. The larger the  $R_i$ , the greater the influence of this factor on the test index. Therefore, the primary-secondary relationship can be quantified based on the primary-secondary relationship of the  $R_i$  judgment factors ( $R_i^*(\%) = R_i / \sum_{i=A}^D R_i$ ). The proportion of the influence of various factors on the various evaluation indexes of CRC can be obtained.

#### (1) CRC compressive strength

It can be seen from Fig. 2 and Table 3 that the influence of each factor on the compression resistance of CRC is as follows:  $B > A > C$ , and the range proportions are 64.12%, 31.55% and 4.32%. With the increase of  $V_B$  content, the compressive strength of CRC first increased and then decreased gradually. The increase and decrease rates of  $B_2$  and  $B_3$  content were 11.79% and 5.67%, respectively. With the increase of  $V_c$  content from  $C_1$  to  $C_3$ , the compressive strength slightly increased by 1.49% and 0.46%, respectively. With the content of  $V_a$  from  $A_1$  to  $A_3$ , the compressive strength showed an increasing trend, and the maximum increase was 11.46% at the content of  $A_2$ .

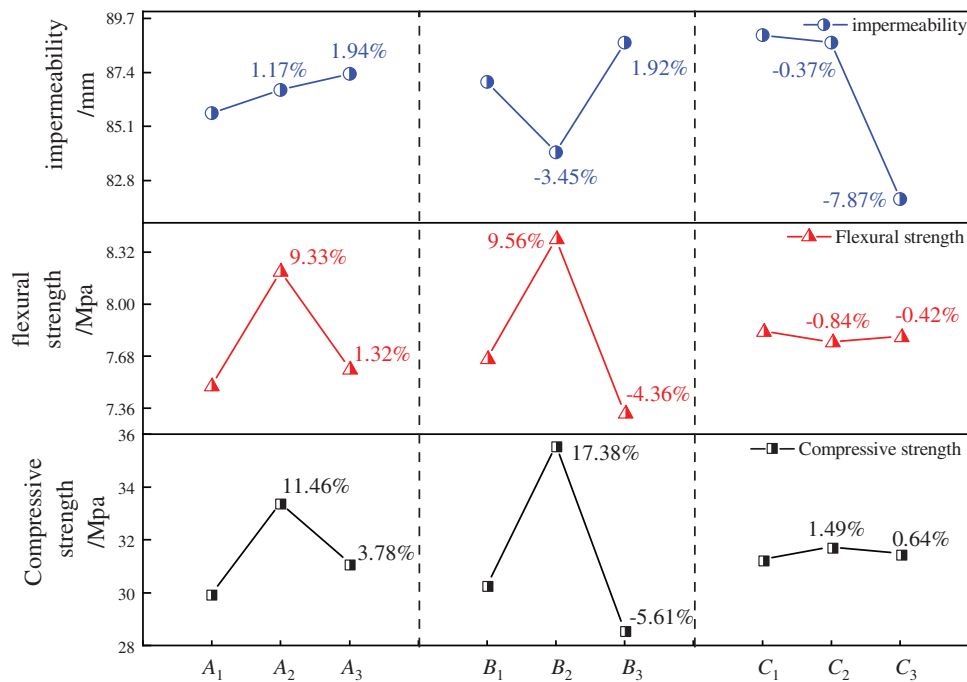


Figure 2: Relationship between factor level and evaluation indexes

#### (2) CRC flexural strength

It can be seen from Fig. 2 and Table 3 that the influence of each factor on the compressive strength of CRC is  $B > A > C$  in descending order, and the range proportions are 52.45%, 39.22% and 8.33%. With the

increase of the content of  $V_a$ , the flexural strength increases gradually, and the maximum increase is 9.33% at the content of  $A_2$ . With the increase of  $V_b$  content, the flexural strength first increased and then decreased, and the increase and decrease of  $B_2$  and  $B_3$  were 9.56% and 4.36%, respectively. With the continuous increase of  $V_c$  content, the flexural strength decreases continuously, and the reductions at  $C_2$  and  $C_3$  are 0.84% and 0.42%, respectively.

### (3) CRC impermeability

It can be seen from Fig. 2 and Table 3 that the influence of each factor on the compressive strength of CRC is  $C > B > A$  in descending order, and the range proportions are 52.47%, 35.01% and 12.52%. With the content of  $V_a$  from  $A_1$  to  $A_3$ , the impermeability of CRC gradually decreased, and the maximum decrease was 1.94% at  $A_3$ . With the continuous increase of  $V_b$  content, the impermeability of CRC increased first and then decreased, and the increase and decrease rates at  $B_2$  and  $B_3$  were 3.45% and 1.92%, respectively. With the content of  $V_c$  from  $C_1$  to  $C_3$ , the impermeability increased continuously, and the maximum increase was 7.87% at the content of  $C_3$ .

#### 3.1.2 Variance Analysis

The variance is calculated according to the existing literature and research methods [29,30]. From Table 4, it can be seen from the F value that the influence order of each factor level on the compressive strength and flexural strength evaluation index of CRC is  $B > A > C$ , and the order of influence on the impermeability performance evaluation index of CRC is  $C > B > A$ . This is consistent with the previous range analysis results. According to the results of current test data and range analysis, the best combination of compressive strength, flexural strength and impermeability of CRC are  $A_2B_2C_2$ ,  $A_2B_2C_3$ ,  $A_3B_2C_2$  and  $A_3B_2C_3$ , respectively. Therefore, the content of rubber with a particle size of 1~3 mm is determined as  $B_2$ . Although  $A$  has a significant effect on the flexural strength of CRC, its flexural strength increases from  $A_2$  to  $A_3$  by only 1.33%, but its impermeability performance decreases by 1.66%. The optimal dosage of  $A$  is determined comprehensively as  $A_2$ . In the same way, the optimal dosage of  $C$  is determined as  $C_3$ . Therefore, the optimum ratio of the three rubbers with particle sizes of 3~5 mm, 1~3 mm and 20 mesh is 2%:5%:10%.

**Table 4:** Variance analysis of test result

Index	Factor	Sum of squares of deviations	Freedom	F value	Significance level	Contribution/%
Compressive strength/MPa	$A$	18.362	2	8.36	(*)	33.52
	$B$	79.162	2	36.06	**	65.74
	$C$	0.507	2	0.15	(*)	0.74
Flexural strength/MPa	$A$	1.140	2	24.43	**	40.08
	$B$	1.786	2	38.29	**	56.91
	$C$	0.006	2	0.14	(*)	3.01
Impermeability/mm	$A$	4.222	2	1.46	(*)	35.45
	$B$	33.556	2	11.62	*	57.27
	$C$	93.556	2	32.38	**	7.28

Note: According to the critical value of F distribution, when  $F > F_{0.05}(2,2) = 19$ , it means that the effect is particularly significant “\*\*\*”. When  $9 = F_{0.1}(2,2) < F < F_{0.05}(2,2) = 19$ , it means the influence is significant “\*”. When  $F < F_{0.1}(2,2) = 9$ , it means the non-significant factor “(\*)” [30].

### 3.2 CRC Performance under Salt Freezing Cycle

#### 3.2.1 Test Ratio

From the above test, it can be determined that the ratio of the combined dosage of the three particle sizes of rubber is 1:2.5:5. In order to further explore the effect of the total dosage on the sulfate resistance of CRC, and to find the optimal total rubber dosage within the volume dosage of 10%~20%, a salt-freezing cycle test was conducted to compare the CRC with the RC. The specific mixing ratio is shown in Table 5.

**Table 5:** Test mix proportion

Number	Rubber dosage/%	Number	Rubber dosage/%
CRC-1	1.2 + 2.9 + 5.9	<b>RC-1</b>	0 + 0 + 12
CRC-2	1.4 + 3.5 + 7.1	<b>RC-2</b>	0 + 10 + 0
CRC-3	1.8 + 4.4 + 8.8	<b>RC-3</b>	5 + 0 + 0
CRC-4	2.1 + 5.3 + 10.6	/	/
CRC-5	2.4 + 5.9 + 11.7	/	/

Note: 1.2 + 2.9 + 5.9 means that the particle size of 3~5 mm, 1~3 mm, and 20 mesh rubber is mixed with 1.2%, 2.9%, and 5.9%, respectively. Other data have the same meaning.

#### 3.2.2 Internal Velocity Acoustic Damage

After each freeze-thaw cycle for 30 times, ultrasonic flaw detection was performed on the specimen to obtain the wave speed of the specimen after being eroded by sulfate, as shown in Fig. 3.

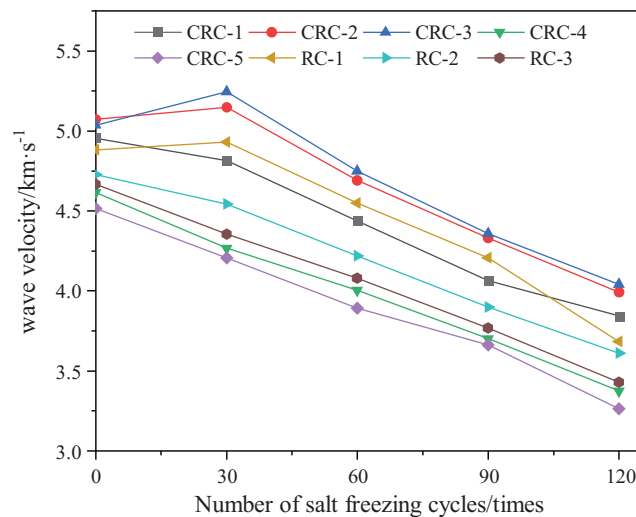


**Figure 3:** Wave velocity after sulfate erosion

It can be seen from Fig. 3 that the acoustic damage of the CRC-2, CRC-3 and RC-1 specimens showed a trend of the first decrease and then increase during the entire freeze-thaw cycle. With the increase of the number of salt-freezing cycles, for the specimens with a rubber content of not more than 10% (CRC-1) and those with a rubber content of more than 15% (CRC-4, CRC-5, RC-2, RC-3), the acoustic damage tends to increase gradually. At the end of the experiment, the wave velocity reductions of CRC-1 to CRC-5 were 22.4%, 21.3%, 19.8%, 26.9%, and 27.7%, respectively, and the wave velocity reductions of

RC-1 to RC-3 were 24.5%, 23.6%, and 26.5%, respectively. CRC-3 has the lowest wave velocity drop and the largest wave velocity.

### 3.2.3 Compressive and Flexural Strength

After each freeze-thaw cycle for 30 times, the compressive and flexural strengths of the specimens were tested, and the results are shown in Figs. 4 and 5.

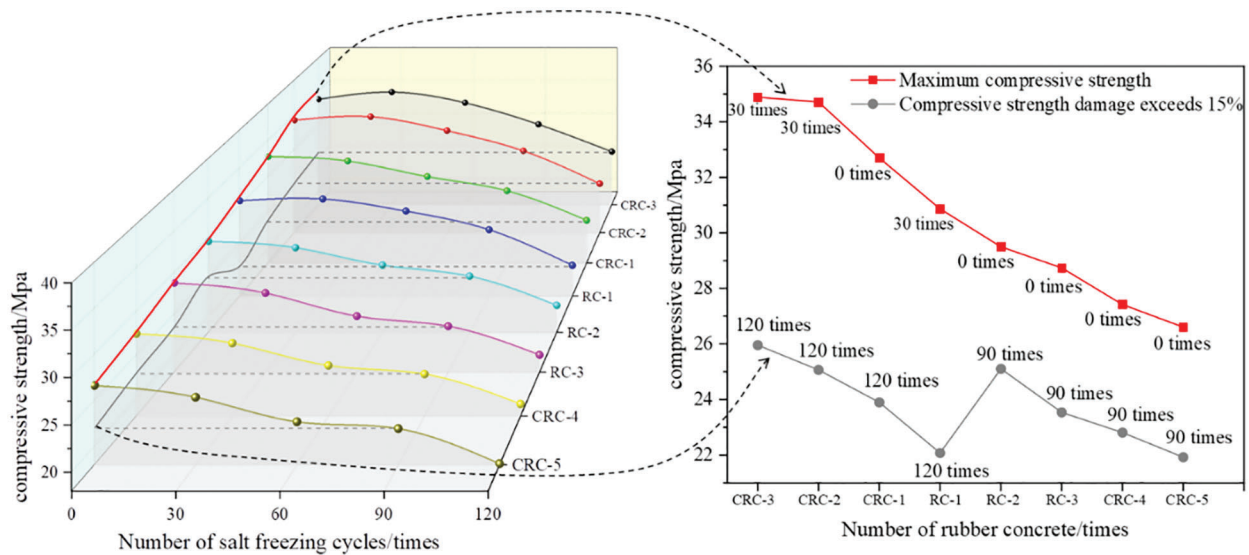


**Figure 4:** Compressive strength after sulfate erosion

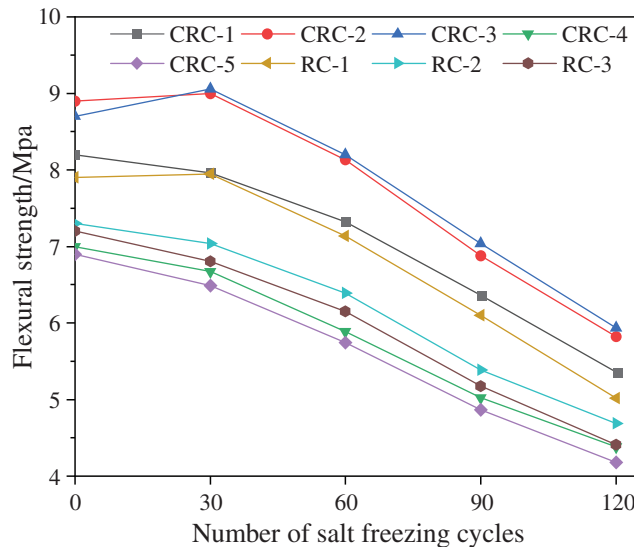


**Figure 5:** Flexural strength after sulfate erosion

As can be seen from the left graph in Fig. 4, after 120 salt-freezing cycles, the compressive strengths of the three RC dosages decreased by 27.9%, 27.4% and 30.1%, respectively, and their compressive strengths were 22.08, 21.42 and 22.10 MPa, respectively. The compressive strength of the other 5 kinds of CRC concrete after 120 salt-freezing cycles decreased by 26.9%, 26.7%, 23.2%, 29.3% and 31.9%,

respectively. After 120 salt-freezing cycles, the compressive strength of CRC with a total content of compound rubber of 10%~15% was higher than that of RC concrete, and the decrease ratio in compressive strength was lower than that of RC concrete. Therefore, it can be obtained that the compressive strength of CRC-3 with a total content of 15% has the lowest decrease ratio in compressive strength and the highest compressive strength after the salt freezing test.

From the right picture in Fig. 4, it can be seen that the maximum compressive strength of CRC-3 and CRC-2 with a compound rubber content of 10%~15% appears after 30 salt-freezing cycles, and the compressive strength increases by 3.2% and 1.5%, respectively. Ultimately, the compressive strength loss exceeded 15% after 120 salt-freezing cycles. However, the maximum compressive strength of CRC-4 and CRC-5 with a large amount of composite rubber appears at the initial moment of the salt-freezing cycle, and the compressive strength decreases with the increasing number of salt-freezing cycles. After 90 salt-freezing cycles, the strength damage reached 16.8% and 17.6%, respectively, both exceeding 15%. For RC-1 with a small rubber particle size and a rubber content of 10%, the maximum compressive value also appeared after 30 salt-freezing cycles, and the compressive strength damage did not exceed 15% after 120 salt-freezing cycles. For the other RC-2 and RC-3 with a larger rubber particle size, their frost resistance and sulfate resistance are weaker than RC-1.

It can be seen from Fig. 5 that the flexural strength of RC and CRC has an obvious decreasing trend. After 120 salt-freezing cycles, the flexural strength of RC decreased by 36.5%, 35.8%, and 38.8%, respectively, while that of CRC was decreased by 34.6%, 34.4%, 31.8%, 37.4%, and 39.4%, respectively. The CRC with a compound content of 15% showed the lowest decrease in flexural strength and the highest flexural strength after salt-freezing cycles. The overall decrease in flexural strength was larger than that in compressive strength, indicating that flexural strength is more sensitive to damage from sulfate attack. The main reason for this phenomenon is that the eroded part is under pressure due to expansion, and tension is generated in the uneroded part. This part of the tension is superimposed with the tension generated by the external load, which eventually leads to a significant decrease in the flexural strength of concrete.

It can be seen from the above analysis that when the rubber particles of 3~5 mm, 1~3 mm and 20 mesh are added in the ratio of 1:2.5:5 and the total amount is 15%, the performance of concrete against sulfate corrosion is better. It is also not negligible that existing studies [14,31] have shown: when the content of 1~3 mm rubber particles is 10%, CRC exhibits the optimal mechanical strength. At the same time, the experimental data in this paper show that the compound blending of rubber particles can increase the optimum blending amount of waste rubber. In later chapters, the mechanism will be revealed in combination with mesoscopic simulations.

## 4 Performance Prediction Model under Salt-Freezing Cycle

### 4.1 The Relationship between Ultrasonic Velocity and Concrete Strength

The microscopic damage caused by crack generation and crack propagation in concrete is reflected by the wave velocity, and the macroscopic performance caused by it is the change of strength. Therefore, the relationship between the wave velocity  $v$  and the compressive strength  $f_c$  and flexural strength  $f_{cf}$  of each group of rubber concrete is made, and an appropriate function is selected for regression analysis. The results are shown in Fig. 6. The form of the fitting function is  $f_c = ae^{bv}$ ,  $f_{cf} = ce^{dv}$ , and the specific fitting parameters are shown in Table 6.

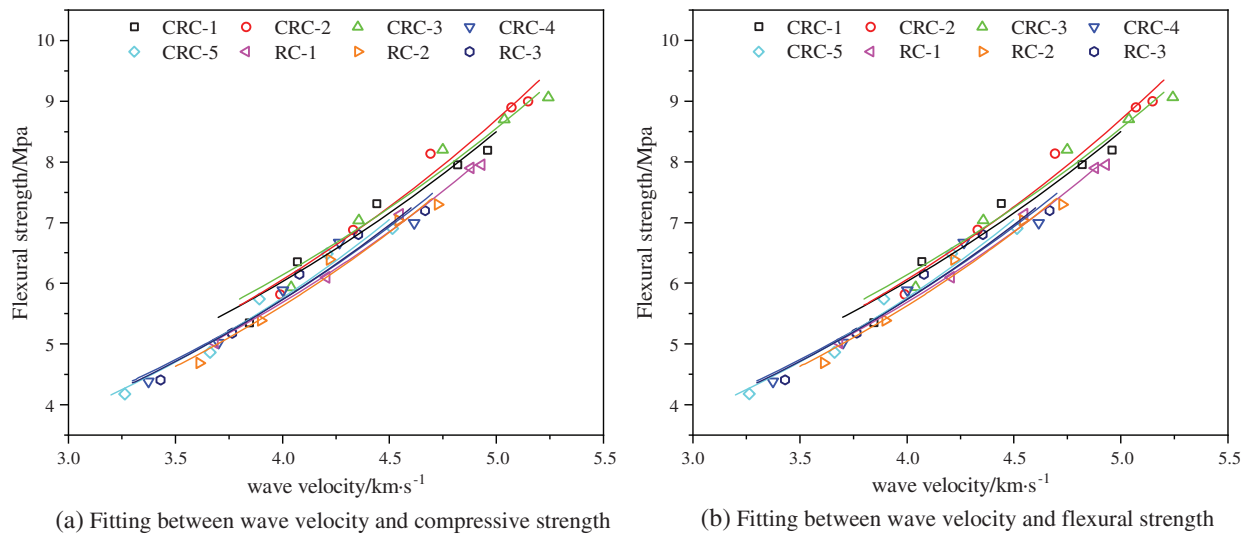


**Figure 6:** Fitting of concrete salt freezing cycle wave velocity with compressive strength and flexural strength

**Table 6:** Fitting results of wave velocity and strength of concrete after salt freezing cycle

	CRC-1	CRC-2	CRC-3	CRC-4	CRC-5	RC-1	RC-2	RC-3
Compressive strength $f_c$ fitting parameters	$a = 9.885$ $b = 0.245$	$a = 9.739$ $b = 0.250$	$a = 11.051$ $b = 0.223$	$a = 8.321$ $b = 0.263$	$a = 7.298$ $b = 0.291$	$a = 8.969$ $b = 0.254$	$a = 8.695$ $b = 0.262$	$a = 8.048$ $b = 0.277$
$R^2$	0.915	0.922	0.909	0.942	0.961	0.960	0.947	0.961
Flexural strength $f_{cf}$ fitting parameters	$c = 1.525$ $d = 0.344$	$c = 1.429$ $d = 0.361$	$c = 1.624$ $d = 0.332$	$c = 1.257$ $d = 0.379$	$c = 1.140$ $d = 0.405$	$c = 1.281$ $d = 0.372$	$c = 1.179$ $d = 0.391$	$c = 1.202$ $d = 0.391$
$R^2$	0.948	0.972	0.949	0.954	0.965	0.994	0.974	0.962

#### 4.2 Salt-Freezing Cycle Strength Damage Model

The generation and expansion of cracks in rubber concrete are related to the number of salt-freezing cycles and the number of rubber particles, resulting in changes in the wave speed and strength parameters of rubber concrete. In order to further explore the relationship between the three, the surface of the rubber content, the number of salt-freezing cycles and the wave speed, compressive strength, and flexural strength of each group of rubber concrete was made, and regression analysis was carried out. The results are shown in Figs. 7–9. The fitting function formula is shown in Table 7.

### 5 Numerical Simulation

#### 5.1 Microscopic Concrete Model

In this paper, a meso-concrete model is established based on Abaqus software and Python that generates and randomly places aggregates. For the study of the mechanical properties of the composite material of rubber concrete, it is necessary to establish a meso-structure model that is close to the real rubber concrete meso-structure in the statistical sense. The establishment of the model is mainly divided into two steps: the generation of random aggregates and the delivery of aggregates.

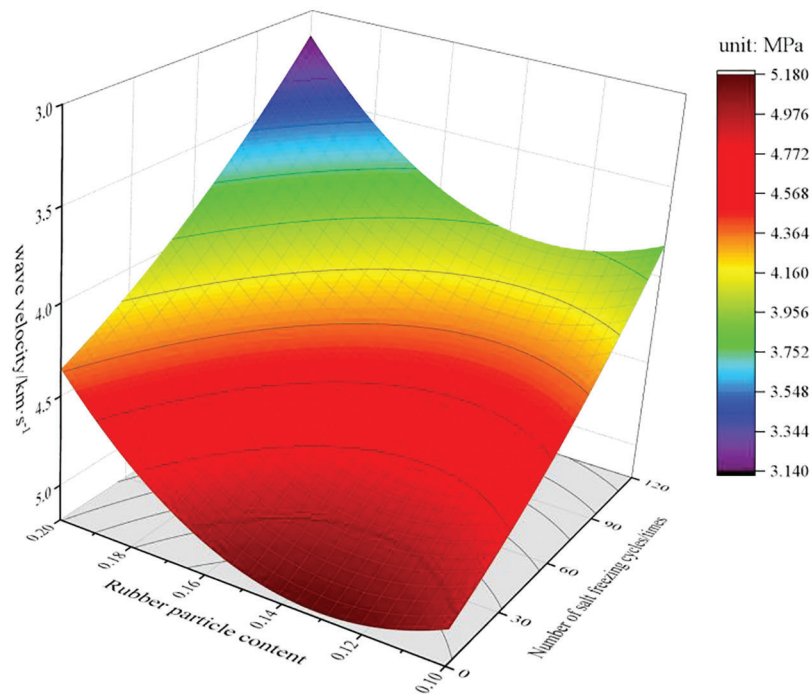


**Figure 7:** Fitting of concrete salt freezing cycle times with rubber output and wave velocity

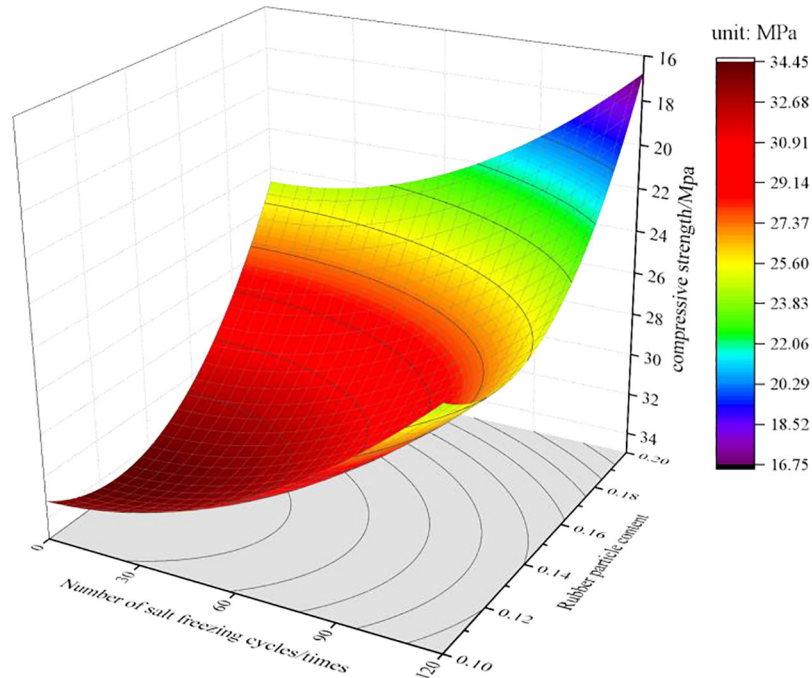


**Figure 8:** Fitting of concrete salt freezing cycle times with rubber output and compressive strength

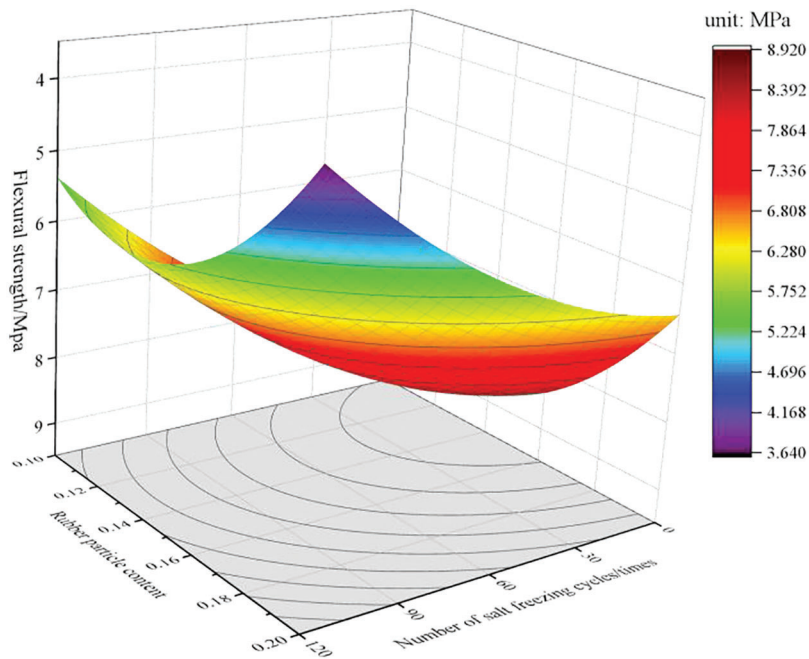


**Figure 9:** Fitting of concrete salt freezing cycle times with rubber output and flexural strength

**Table 7:** Fitting results of rubber content, salt freezing cycle times, wave velocity and strength

Strength parameters	Fitting equation	$R^2$
Compressive strength $f_c$	$f_c = 5.511 + 457.1m - 0.01367n - 1806m^2 + 0.08527mn - 0.00058n^2$	0.912
Flexural strength $f_{cf}$	$f_{cf} = 0.8398 + 125.1m - 0.01114n - 485.2m^2 + 0.2579mn - 0.00015n^2$	0.915
Wave velocity $v$	$v = 2.164 + 45.76m - 0.005815n - 174.1m^2 - 0.003017mn - 0.00003n^2$	0.923

Note:  $n$  is the number of salt-freezing cycles,  $m$  is the rubber content.

### 5.1.1 Random Aggregate Generation

As a stochastic simulation method, Monte Carlo method originates from the mathematical idea of approximating probability with probability, and is mainly used to solve uncertain problems with randomness [32]. For example, when the reliability characteristics of each unit in the system are known, but the system is too complex to obtain a reliable mathematical model, the stochastic simulation method can be used to approximate the predicted value of the system reliability. For the mesoscopic model of rubberized concrete, the shape, size and distribution position of rubber particles in concrete are all random, and these characteristics are difficult to describe with an accurate mathematical model. However, regardless of the shape, size or position of rubber particles, there are certain statistical laws, and the use of distribution functions derived from statistical laws to characterize them is the main method of mesoscopic simulation at present. Therefore, this study simulates the generation and placement of rubber particles in the mesoscopic model of rubber concrete based on the Monte Carlo method.

The random variables of the shape, size and position distribution of rubber particles need to be realized by random numbers. This study uses the rand command in Python to generate a random number  $x$  on the interval  $[0,1]$ , and then generates a random number distributed in the given interval through

transformation. If you want to get the random number  $x'$  on the interval  $[a,b]$ , you can get it by transforming the following equation:

$$x' = a + (b - a)x \quad (4)$$

### 5.1.2 Delivery of Random Aggregates

In the Cartesian coordinate system, for a random polygonal aggregate placed in a square area, its centroid coordinates can be expressed as:

$$x = x_{\min} + \lambda(x_{\max} - x_{\min}) \quad (5)$$

In the formula:  $x$  is the centroid coordinate vector,  $x_{\max}$  and  $x_{\min}$  are the boundary positions of the concrete sample.  $\lambda$  is a random number for each of the two directions, and the value is between 0~1.

The aggregates are randomly distributed inside the specimen and do not contact each other. The minimum thickness between the aggregate particles and the boundary of the concrete specimen is taken as the times of the minimum size of the aggregate, and a value of  $\lambda$  is initially selected according to the aggregate content. When there is difficulty and cannot be completed, the delivery process can be completed by continuously reducing the value of  $\lambda$ .

## 5.2 Methods for Simulating Cracks

In the process of concrete stress, the internal micro-cracks begin to expand and aggregate, resulting in continuous damage to the concrete. In the finite element method, the appearance of cracks leads to strong discontinuities, which increases the computational cost dramatically. In order to simulate cracks accurately and efficiently, many crack models have been proposed, mainly continuous crack model, discrete crack model and cohesive crack model [33].

In the cohesive crack model, a zero-thickness cohesive element (Cohesive element) is embedded in the boundary of the conventional finite element, so that the nodes are separated and the displacement is discontinuous during the loading process. The model adopts the separation method to simulate the crack, and realizes the simulation of the continuous loss of energy during the fracture process based on the attenuation relationship between the traction force and the separation displacement during the cracking process. Due to the above characteristics, this model is widely used in the numerical simulation of concrete cracking [34,35]. A cohesive crack model based on the traction-separation law is built into the large-scale general finite element software Abaqus. Therefore, based on Abaqus software, this paper adopts the cohesive crack model to simulate the whole process of crack development.

### 5.3 Cohesive Element Constitutive Model

The two-dimensional bonding element COH2D4 in Abaqus software has four nodes, each node has 2 degrees of freedom, as shown in Fig. 10. The traction-separation law describes the relationship between the relative displacement and stress between planes 1–2 and planes 3–4, that is, the element only has tensile deformation along the  $n$ -direction and shearing deformation along the  $t$ -direction.

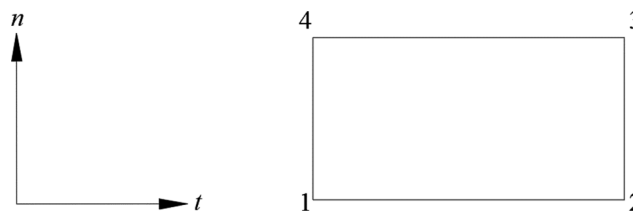


**Figure 10:** Schematic diagram of two-dimensional bonding element

The relationship between stress and relative displacement in each direction of the element is:

$$t = \begin{Bmatrix} t_n \\ t_t \end{Bmatrix} = (1 - D) \begin{bmatrix} K_{nn} & K_{nt} \\ K_{tn} & K_{tt} \end{bmatrix} \begin{Bmatrix} \delta_n \\ \delta_t \end{Bmatrix} \quad (6)$$

$$\varepsilon_n = \frac{\delta_n}{T_0}, \varepsilon_t = \frac{\delta_t}{T_0} \quad (7)$$

where:  $t_n, t_t$  are the stress components in the  $n$  and  $t$  directions, respectively.  $\delta_n, \delta_t$  is the corresponding displacement component.  $K_{ij}$  is the displacement in the  $j$  direction vs. the stress stiffness in the  $i$  direction.  $T_0$  is the thickness of the unit layer, and  $T_0 = 1$  is often taken in the actual calculation.  $D$  is the degree of damage.

This simulation does not consider the coupling effect of stress components in all directions, so the elements outside the main diagonal in Eq. (6) are all zeros.

## 5.4 Damage and Failure of Cohesive Elements

### 5.4.1 Initial Damage Criterion

The element begins to suffer initial damage when the stress or strain reaches the initial damage criterion as the load continues to be applied. The model established this time is mainly used to simulate the cracking behavior of rubber concrete under the action of compressive stress, so the quadratic stress criterion (Quads) is adopted, that is, when the traction force satisfies the Eq. (8), the damage starts

$$\left\{ \frac{\langle t_n \rangle}{t_{n0}} \right\}^2 + \left\{ \frac{t_s}{t_{s0}} \right\}^2 = 1 \quad (8)$$

where:  $\langle \rangle$  is the Macaulay operator

$$\langle t_n \rangle = \begin{cases} t_n & t_n > 0(\text{tension}) \\ 0 & t_n < 0(\text{compression}) \end{cases} \quad (9)$$

### 5.4.2 Linear Damage Evolution Model

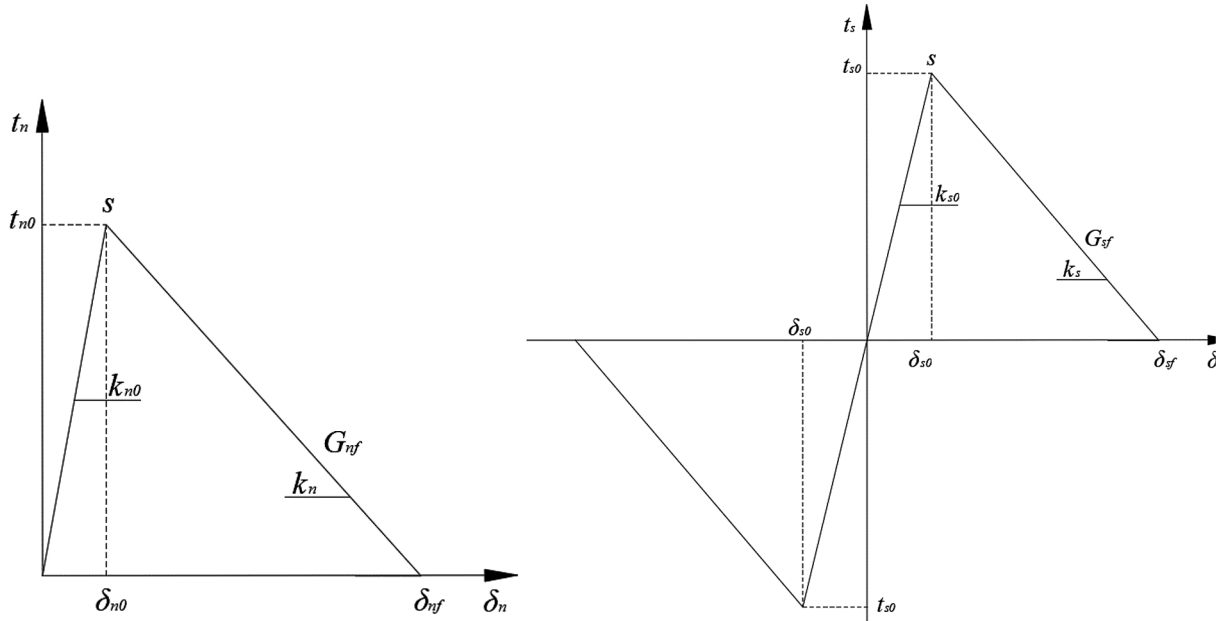
After the initial damage of the bonded element, if it is further stressed, it will enter the damage evolution stage until it fails completely. The stress-displacement relationship of the viscous element in the damage evolution stage is described by the damage evolution model, and many scholars have tried different damage evolution models to simulate the fracture behavior of concrete [36–41].

In this paper, based on the existing research [42], the single-linear damage evolution model is used to study the cracking of concrete. Fig. 11 shows the relationship between the normal and tangential traction and displacement, respectively. The normal feature describes the I-type opening mode of the crack,  $G_{nf}$  is the I-type fracture energy,  $t_{n0}$  is the normal bond strength, and  $\delta_{nf}$  is the normal complete separation displacement. The tangential feature describes the type II slip mode of the crack,  $G_{sf}$  is the type II fracture energy,  $t_{s0}$  is the tangential bond strength, and  $\delta_{sf}$  is the tangential complete separation displacement.

$$G_{\alpha f} = \int_0^{\delta_{\alpha f}} t_{\alpha}(\delta) d\delta = \frac{1}{2} t_{\alpha 0} \delta_{\alpha f} \quad (10)$$

When  $\alpha = n$ , it represents the normal bonding law. When  $\alpha = s$ , it means the law of tangential bonding. In general, the separation displacement is difficult to measure, so fracture energy and bond strength are often used as the parameters of the bond relationship. From Eq. (10), if the fracture energy of the material is  $G_{\alpha f}$ , the complete separation displacement can be expressed as:

$$\delta_{\alpha f} = 2G_{\alpha f}/t_{\alpha 0} \tag{11}$$



(a) Normal traction-displacement relationship of bonding element

(b) Tangential traction displacement relationship of bonding element

**Figure 11:** The relationship between the traction force and the displacement of the bonding element

The equivalent separation displacement of the bonding unit can be expressed as:

$$\delta_c = \sqrt{\langle \delta_n \rangle^2 + \delta_s^2} \tag{12}$$

$$\langle \delta_n \rangle = \begin{cases} \delta_n, & \delta_n \geq 0 \text{ (tension)} \\ 0, & \delta_n \leq 0 \text{ (compression)} \end{cases} \tag{13}$$

The damage degree  $D$  of the bonding unit can be determined according to the Eq. (14):

$$D = \frac{\delta_e^f (\delta_e^{max} - \delta_e^0)}{\delta_e^{max} (\delta_e^f - \delta_e^0)} \tag{14}$$

where:  $\delta_e^f$ — Completely equivalent separation displacement

$\delta_e^{max}$ — Maximum equivalent separation displacement in load history

$\delta_e^0$ — Equivalent separation displacement at bond strength

The value range of the damage degree  $D$  can be obtained from the Eq. (14) is 0–1.

### 5.5 Damage Variable

Crack nucleation and propagation are the root causes of damage and failure of rubber concrete. In the cohesive crack model, the ratio of the number of completely separated bond elements  $N_s$  to the total number of bond elements  $N_c$  is defined as the microcrack ratio  $\lambda_c(t)$ . When  $D > 0.90$ , the bonding element is considered to be completely separated.

$$\lambda_c(t) = \frac{N_s(t)}{N_c}$$

### 5.6 Nonlinear Problem Solving Methods

The failure and cracking of concrete involved in this simulation is a highly nonlinear problem, and convergence problems are usually encountered when using Abaqus/Standard (implicit statics) to solve. Using Abaqus/Explicit (explicit dynamics) can effectively solve highly nonlinear problems.

### 5.7 Uniaxial Compression Simulation of Rubber Concrete

#### 5.7.1 Model Parameters

A 100 mm × 100 mm two-dimensional concrete mesoscopic specimen was established. The specimen number and rubber content are shown in Table 5. After meshing the sample and embedding zero-thickness viscous elements, assigning corresponding material properties to each element set is necessary. The specific material parameters are shown in Table 8. The linear quadrilateral plane stress element (CPS4) is used to solve the problem using Abaqus/explicit.

**Table 8:** Material parameters of meso model

	Elastic Modulus $E$ (MPa)	Poisson's ratio $\mu$	Density $\rho$ ( $10^{-9}$ t/mm <sup>3</sup> )
Rubber	6.1	0.47	1.0
Mortar	26,500	0.2	2.4
Rubber bonding element	/	/	1.0
Mortar bonding element	/	/	2.4
interface bonding element	/	/	2

The boundary conditions are shown in Fig. 12. The upper and lower steel plates of the specimen are considered as rigid bodies in the simulation, the vertical and horizontal displacements of the lower steel plate are constrained, and 1mm displacement is applied to all nodes of the upper steel plate. Meshing (taking CRC-3 as an example) is shown in Fig. 13.

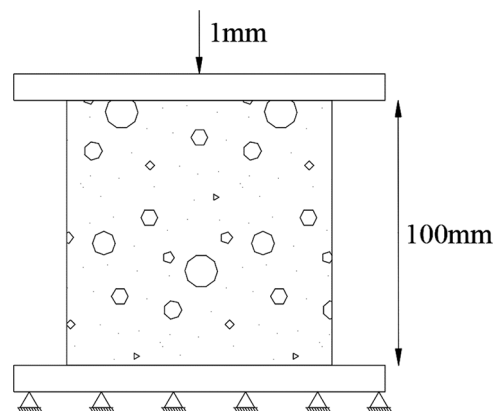


**Figure 12:** Boundary conditions of uniaxial fracturing simulation

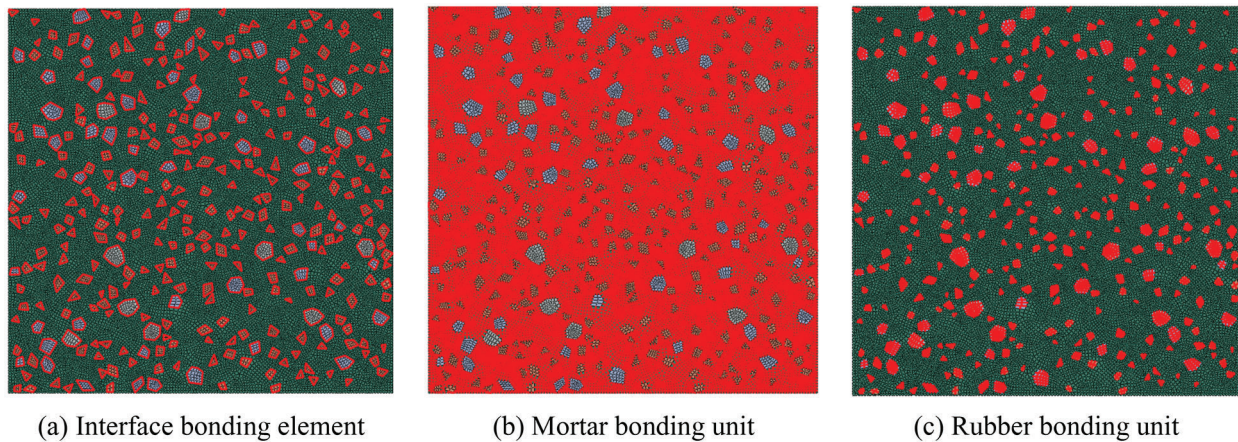


**Figure 13:** Grid division diagram of CRC-3 sample

### 5.7.2 Model Damage Analysis

Taking the micro-crack ratio defined in Section 5.5 as the damage variable, the state of the bond unit and the crack propagation in the meso-model under compression were recorded. The meso-mechanism of the damage of rubber concrete is further explored by correlating the damage of the bonding unit with the overall mechanical behavior of rubber concrete. Figs.14–17 are respectively the propagation diagrams of cracks when CRC-3, RC-1, RC-2, and RC-3 finally fail. It can be seen from Figs. 14 and 16 that both CRC-3 and RC-2 have 3 main cracks when they are finally broken, CRC-3 has multiple microcracks, while RC-2 has fewer microcracks. However, RC-1 and RC-3 had two main cracks when they finally failed, and there were few microcracks in both. Therefore, the damage modes of CRC-3 and RC-2 are defined as damage mode A, and the damage modes of RC-1 and RC-3 are defined as damage mode B. Macroscopic damage can be roughly divided into three stages.

- (1) Microcrack nucleation and growth stages. Before the peak stress, microcracks are generated at the interface and are randomly distributed. As shown in Figs. 14a and 15a.
- (2) Microcrack connection and propagation stage. After reaching the peak stress, the cracks generated at the interface between the rubber and the mortar continue to expand and connect to each other along the interface, resulting in larger-scale damage. As shown in Figs. 14b and 15b.
- (3) Crack polymerization stage. The main crack continued to expand and aggregated leading to the final failure of the specimen. Damage mode A forms two main cracks, as shown in Fig. 15c. On the other hand, damage mode B forms three main cracks, as shown in Fig. 14c.

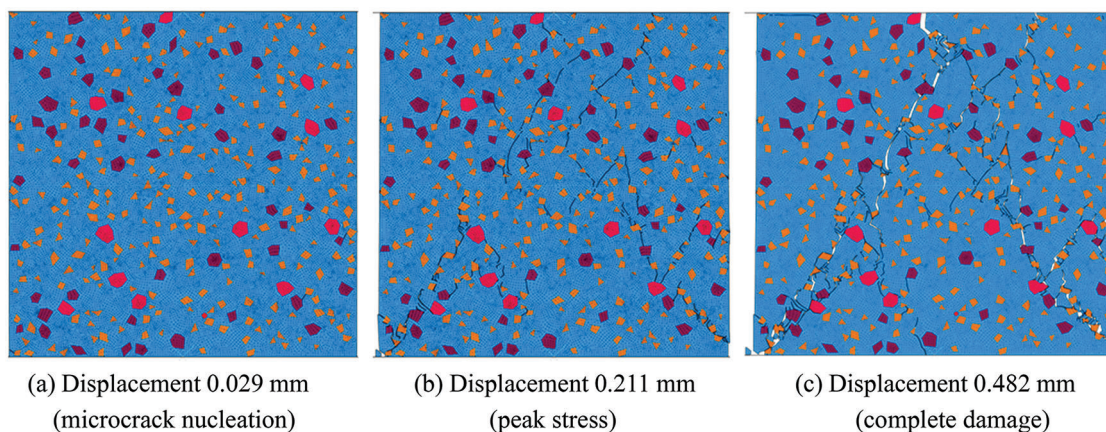


**Figure 14:** Crack distribution diagram of CRC-3 model failure process

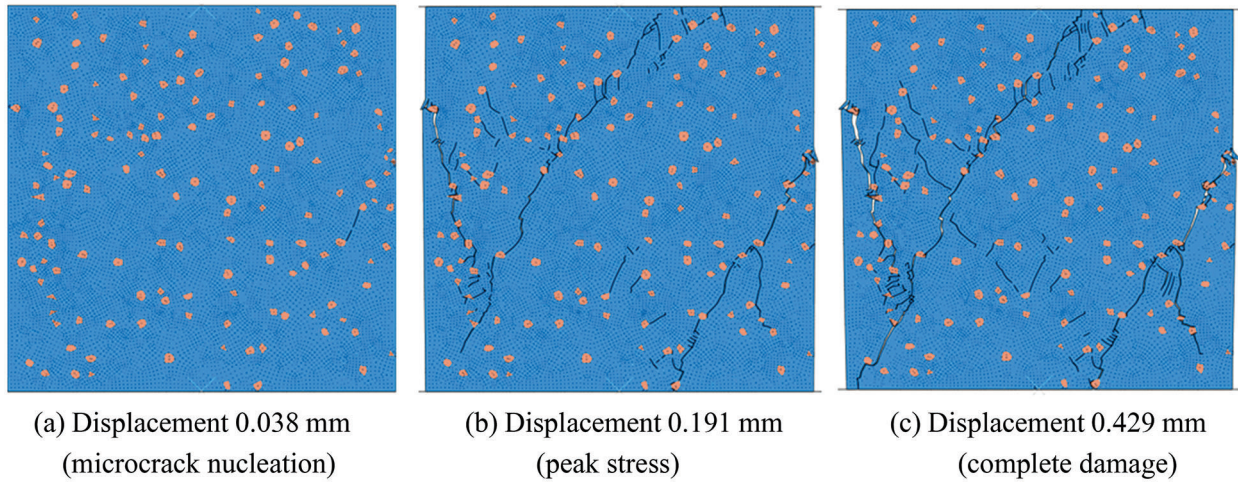


**Figure 15:** Distribution of cracks in the failure process of RC-1 model

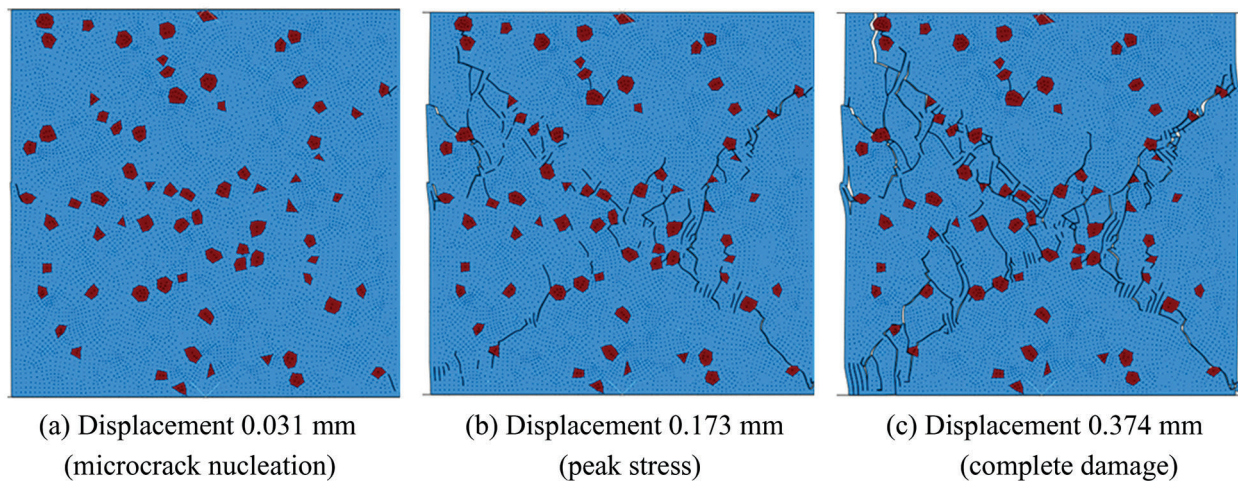


**Figure 16:** Distribution of cracks in the failure process of RC-2 model

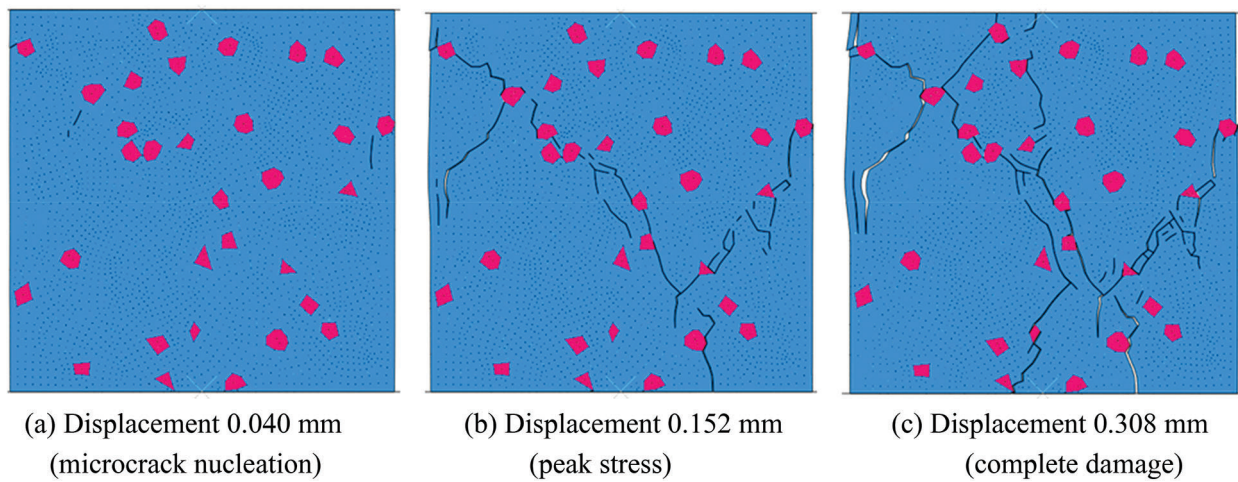


**Figure 17:** Distribution of cracks in the failure process of RC-3 model

Through the relationship between the average stress, the proportion of microcracks and the loading displacement, the mesoscopic damage mechanism of the three stages is further analyzed. Fig. 18 is the relationship curve of the average stress, the proportion of microcracks and the loading displacement corresponding to CRC-3, RC-1, RC-2 and RC-3, respectively. The average stress is the ratio of the reaction force of the upper steel plate to the size of the sample, and the displacement is the displacement of the upper loading. The microscopic damage analysis of each stage is as follows:

- (1) Linear segment AB: Damage modes A and B can be clearly observed in this stage without micro-crack nucleation, and the average stress and displacement curves have a linear relationship. As the displacement continues to increase, the concrete begins to be damaged. At this time, the corresponding stresses are 12.17, 11.33, 10.32 and 10.92 MPa, which are about 36% of their peak stress.
- (2) Nonlinear segment BC: The proportion of microcrack nucleation increases rapidly. For damage mode B, there is an obvious yield plateau. The peak stresses of CRC-3 and RC-2 are 33.21 and 29.41 MPa, respectively. When the peak stress is reached, the proportion of microcracks is basically the same, which is 51% and 48%, respectively. For damage mode A, there is no obvious yield plateau, the peak stress of RC-1 and RC-3 are 30.52 and 28.60 MPa, respectively, and the proportion of microcracks corresponding to the peak stress is 47% and 46%, respectively.
- (3) Softening segment CD: For both damage modes, softening begins after peak stress. For damage mode A, the proportion of microcracks increases slowly, and the proportion of microcracks in CRC-3 and RC-2 is 58% and 51% at the final failure. For damage mode B, the proportion of microcracks tends to be stable, and the proportions of microcracks in RC-1 and RC-3 are 53% and 49% at the final failure.

Observing the picture of the damage process of the sample and the form of the microscopic curve, it can be found that there is obvious microcrack nucleation to the expansion stage in the concrete damage process, but there is a big difference in the degree of crack polymerization in the final failure. Compared with RC-1 and RC-3, there are rubber particles with uniform gradation in CRC-3. Larger particles of rubber can prevent cracks polymerization, and small particles of rubber prevent the expansion of microcracks. When the displacement reaches 0.48 mm, the final failure of CRC-3 occurs. The proportion of microcracks is relatively large, and there are three main cracks at the same time. Compared with RC-2, the proportion of microcracks in CRC-3 is slightly larger, and the degree of polymerization of cracks is lower due to the uniform internal gradation of rubber particles, and the yield plateau is more obvious.

## 6 Influence Mechanism of Compound Rubber on Mechanical and Durability Performance of CRC

The research on the influence of rubber particles on the mechanical strength and durability of concrete shows that the higher elastic modulus of rubber particles in rubber concrete can significantly improve the linear expansion coefficient of the matrix, and the mechanical properties of rubber concrete under dynamic loads have been significantly improved. Moreover, the uneven surface of the rubber particles will introduce a certain amount of air [43–45], which will increase the air content of the concrete, reduce its thermal conductivity, and enhance the frost resistance.

The incorporation of rubber particles into the concrete matrix improves the linear expansion coefficient while reducing its mechanical strength, and there is always a “threshold” for the rubber content. Therefore, under the same rubber volume replacement rate, as the particle size of the rubber particles increases, the smaller-sized rubber particles are more likely to be evenly distributed inside the concrete matrix. Therefore, the expansion internal stress caused by sulfate erosion is buffered by the uniform elastic deformation of the small-sized rubber particles. As shown on the left side of Fig. 19.

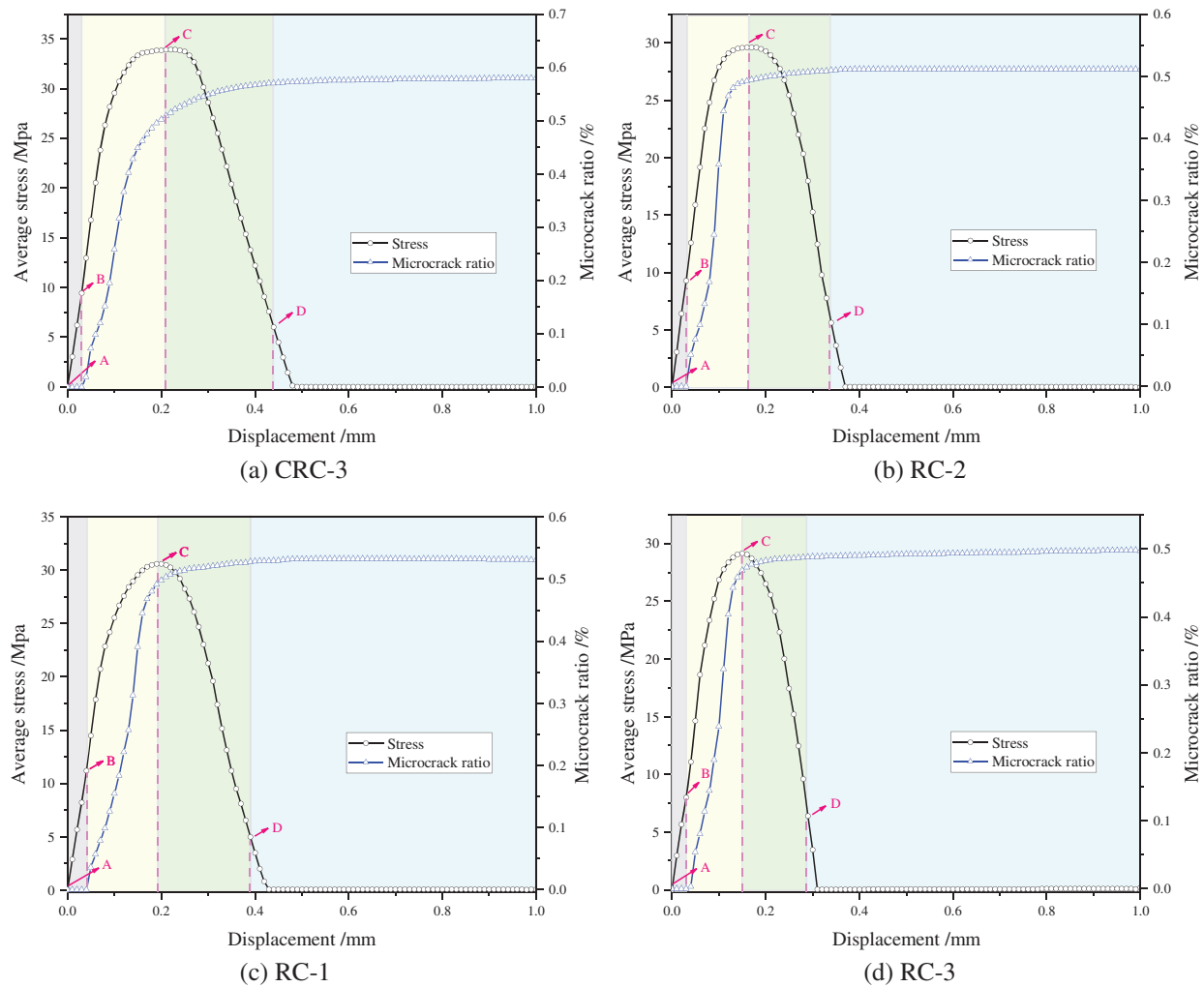


**Figure 18:** Variation of average stress and microcrack density with displacement

Studies have shown that large-diameter rubber particles can improve the erosion resistance of concrete within a certain dosage range [46]. Compared with the small-sized rubber particles, on the one hand, the large-sized rubber particles can introduce more air bubbles to provide a permeation path for the unfrozen solution. In addition, the rubber particles and the introduced closed air bubbles can inhibit the connectivity of the internal pores of the concrete, so that the connected pores become closed pores, and the frost resistance of the concrete is improved. On the other hand, due to the poor dispersibility of large-diameter rubber particles, the introduced air bubbles are not uniform, resulting in an increase or decrease in the penetration path of the solution, which ultimately reduces the frost resistance of concrete. Moreover, the interface between the large-diameter rubber particles and the concrete is more likely to generate stress concentration under the salt-freezing cycle, which accelerates the generation and expansion of micro-cracks, and reduces the integrity of the concrete. As shown on the right side of Fig. 19.

According to the main mechanism of sulfate attack on concrete is the generation of microcracks, crack propagation and aggregation, the crack propagation of composite rubber concrete is simulated by mesoscopic model. At the same time, the results of the previous macroscopic experiments show that due to the compound incorporation of rubber particles, the optimal amount of waste rubber is increased. It can be seen from the

numerical simulation results that not only the large-diameter rubber particles can prevent the penetration of cracks, but also the small-diameter rubber particles can effectively improve the concrete matrix interface in the composite rubber concrete. The combination of large particle size and small particle size rubber particles plays a role in relieving the expansion stress of the matrix and weakening the crack polymerization, and then it is concluded that the composite rubber can effectively improve the sulfate corrosion resistance of concrete. Therefore, compared with RC, CRC not only shows good durability, but also has more advantages in improving the continuous utilization and overall content of waste rubber particles.

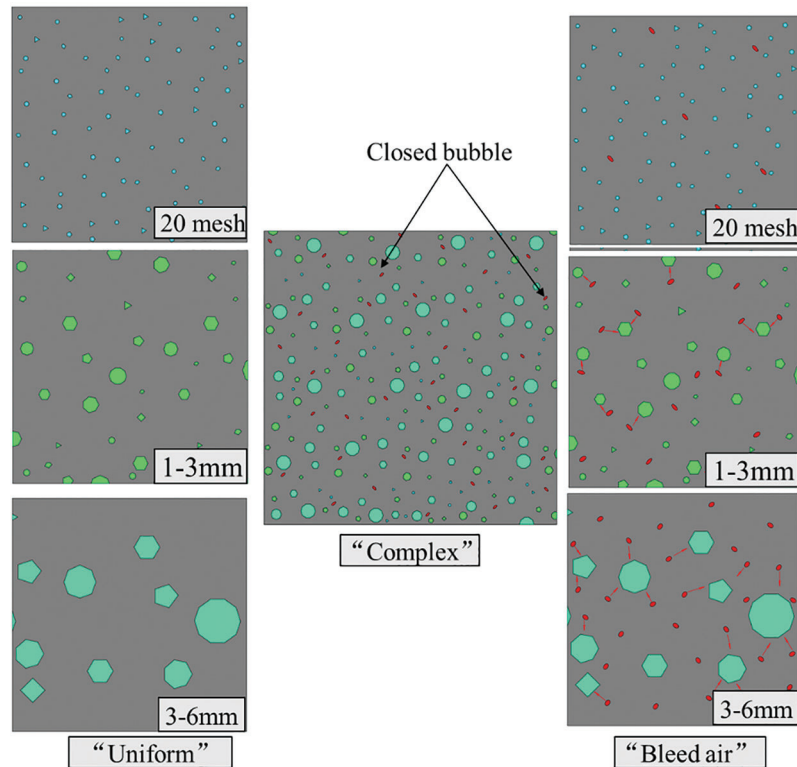


**Figure 19:** Schematic diagram of the microscopic mechanism of compound rubber

## 7 Conclusion

In this paper, CRC was prepared by combining rubber particles with different particle sizes, and the performance of CRC under salt freezing cycle was studied. The following conclusions can be drawn:

- (1) The influence degree of different particle sizes of rubber particles in the orthogonal experimental design on the mechanical properties and impermeability of composite rubber concrete (CRC) are  $1-3 \text{ mm} > 3-5 \text{ mm} > 20$  and  $20 \text{ mesh} > 1-3 \text{ mm} > 3-5 \text{ mm}$ . Through the test data, range analysis and variance analysis, the optimal proportion of 3~5 mm particle size, 1~3 mm particle size and 20 mesh particle size is 1:2.5:5.
- (2) Comparing various ratios of CRC and ordinary single-mixed rubber concrete (RC), the wave velocity changes are basically the same. The addition of rubber particles can improve the corrosion resistance of concrete by sulfate ions, and the wave velocity of the test block after 120 salt-freezing cycles has a minimum decrease of 19.8%. Incorporating particles of different rubber particle sizes into the CRC produces a “gradation-like” effect, forming a stretchable

particle population and introducing uniform bubbles. This changes the internal pore structure, and shows better mechanical properties and sulfate corrosion resistance than ordinary RC.

- (3) The change process of compressive and flexural strength of CRC and RC under sulfate attack is positively correlated with the change of wave velocity. The CRC-3 with the lowest wave velocity loss rate had the lowest compressive and flexural strength reductions of 23.2% and 31.8%, respectively, after 120 salt-freezing cycles. Compared with ordinary RC, the compressive and flexural strengths of the rubber particles of different particle sizes are improved. Based on the test data and analysis results, the ratio of CRC-3 specimens showed good performance. That is, the total volume of the rubber is 15%, and the particle size is 3~5 mm, 1~3 mm, and 20 mesh. That is, the total volume of the rubber is 15%, and the compound rubber is formulated according to the ratio of 1:2.5:5 (3~5 mm:1~3 mm:20 mesh), and the CRC performance is the best.
- (4) The numerical simulation results show that the concrete damage process has obvious microcrack nucleation to the expansion stage, the large particle rubber can prevent the crack from penetrating, and the small particle rubber can prevent the microcrack from expanding. The uniformly graded rubber particles inside make the degree of crack polymerization lower and the yield plateau more obvious.

**Acknowledgement:** The authors are grateful for the financial support from the National Key Research and Development Program of China under the Grant No. 2018YFC0809400.

**Funding Statement:** This study is supported by the National Key Research and Development Program of China under the Grant No. 2018YFC0809400.

**Conflicts of Interest:** The authors declare that they have no conflicts of interest to report regarding the present study.

## References

1. Irina, G., Aleksandr, K., Marina, K., Larisa, R., Iakov, V. (2019). End of life tires as a possible source of toxic substances emission in the process of combustion. *Resources*, 8(2), 113. DOI 10.3390/resources8020113.
2. Amir, R., Thomas, J. R. (2016). Scrap tyre management pathways and their use as a fuel—A review. *Energies*, 9(11), 888. DOI 10.3390/en9110888.
3. Xu, J., Yao, Z. Y., Yang, G., Han, Q. (2020). Research on crumb rubber concrete: From a multi-scale review. *Construction and Building Materials*, 232(10), 117282. DOI 10.1016/j.conbuildmat.2019.117282.
4. Youssf, O., Elchalakani, M., Hassanli, R., Roychand, R., Zhuge, Y. et al. (2022). Mechanical performance and durability of geopolymer lightweight rubber concrete. *Journal of Building Engineering*, 45(12), 103608. DOI 10.1016/j.jobbe.2021.103608.
5. Mhaya, A. M., Fahim, H. G., Faridmehr, I., Razin, Z. A. A., Alyousef, R. et al. (2021). Evaluating mechanical properties and impact resistance of modified concrete containing ground Blast Furnace slag and discarded rubber tire crumbs. *Construction and Building Materials*, 295(1), 123603. DOI 10.1016/j.conbuildmat.2021.123603.
6. Ali, A. S., Hasan, T. M. (2019). Properties of different types of concrete containing waste tires rubber—a review. *IOP Conference Series: Materials Science and Engineering*, 584(1), 479–489. DOI 10.1088/1757-899X/584/1/012051.
7. Nelson, F. M., Reyes, G., Iman, H., Kypros, P., Maurizio, G. et al. (2018). Composites with recycled rubber aggregates: Properties and opportunities in construction. *Construction and Building Materials*, 188(1–2), 884–897. DOI 10.1016/j.conbuildmat.2018.08.069.
8. Trilok, G., Salman, S., Ravi, K. S., Sandeep, C. (2021). Investigating mechanical properties and durability of concrete containing recycled rubber ash and fibers. *Journal of Material Cycles and Waste Management*, 23(3), 1048–1057. DOI 10.1007/s10163-021-01192-w.

9. Guo, J. Q., Huang, M., Huang, S. X., Wang, S. (2019). An experimental study on mechanical and thermal insulation properties of rubberized concrete including its microstructure. *Applied Sciences*, 9(14), 2943. DOI 10.3390/app9142943.
10. Yang, L., Xu, Z., Wang, R. J., Yan, L. (2019). Performance enhancement of rubberised concrete via surface modification of rubber: A review. *Construction and Building Materials*, 227(1), 116691. DOI 10.1016/j.conbuildmat.2019.116691.
11. Guo, Q. L., Michael, A. S., Gregory, G., John, E., Christopher, A. et al. (2004). Development of waste tire modified concrete. *Cement and Concrete Research*, 34(12), 2283–2289. DOI 10.1016/j.cemconres.2004.04.013.
12. Alireza, K., Tuan, D. N., Prashastha, H., Ailar, H. (2018). Effects of surface treatments of recycled tyre crumb on cement-rubber bonding in concrete composite foam. *Construction and Building Materials*, 171(1), 467–473. DOI 10.1016/j.conbuildmat.2018.03.163.
13. Toutanji, H. A. (1996). The use of rubber tire particles in concrete to replace mineral aggregates. *Cement and Concrete Composites*, 18(2), 135–139. DOI 10.1016/0958-9465(95)00010-0.
14. Al-Tayeb, M. M., Abu Bakar, B. H., Akil, H. M., Ismail, H. (2012). Effect of partial replacements of sand and cement by waste rubber on the fracture characteristics of concrete. *Polymer-Plastics Technology and Engineering*, 51(6), 120–123.
15. Osama, Y., Julie, E. M., Tom, B., Yan, Z., Xing, M. et al. (2020). Development of crumb rubber concrete for practical application in the residential construction sector—design and processing. *Construction and Building Materials*, 260(2), 119813. DOI 10.1016/j.conbuildmat.2020.119813.
16. Xu, J., Niu, X., Yao, Z. (2021). Mechanical properties and acoustic emission data analyses of crumb rubber concrete under biaxial compression stress states. *Construction and Building Materials*, 298(3), 123778. DOI 10.1016/j.conbuildmat.2021.123778.
17. Al-Tayeb, M. M., Abu Bakar, B. H., Akil, H. M., Ismail, H. (2012). Effect of partial replacements of sand and cement by waste rubber on the fracture characteristics of concrete. *Polymer-Plastics Technology and Engineering*, 51(6), 583–589. DOI 10.1080/03602559.2012.659307.
18. Zhang, Y., Wang, C., Lu, Y., Ma, A. (2010). Comparison of the fracture process of the rubberized concrete and plain concrete under bending load. *Science China Technological Sciences*, 53(6), 1526–1533. DOI 10.1007/s11431-010-3143-0.
19. Ali, E. A., Modarres, A. (2021). Impact of crumb rubber particles on the fracture parameters of concrete through WFM, SEM and BEM. *Construction and Building Materials*, 305(8), 124693. DOI 10.1016/j.conbuildmat.2021.124693.
20. Xu, J. H., Feng, X. T., Chen, S. L., Shi, C. Y. (2012). Fundamental mechanical performances of rubber concrete. *Applied Mechanics and Materials*, 193, 1401–1404. DOI 10.4028/www.scientific.net/AMM.193-194.1401.
21. Chen, H. L., Li, D. D., Ma, X., Zhong, Z., El-Sayed, A. (2021). Mesoscale analysis of rubber particle effect on young's modulus and creep behaviour of crumb rubber concrete. *International Journal of Mechanics and Materials in Design*, 17(3), 659–678. DOI 10.1007/s10999-021-09552-y.
22. Guo, Q., Wang, S., Zhang, R. (2022). Intrinsic damage characteristics for recycled crumb rubber concrete subjected to uniaxial pressure employing cohesive zone model. *Construction and Building Materials*, 317(2), 125773. DOI 10.1016/j.conbuildmat.2021.125773.
23. Zhou, W., Tang, L., Liu, X., Ma, G., Chen, M. (2016). Mesoscopic simulation of the dynamic tensile behaviour of concrete based on a rate-dependent cohesive model. *International Journal of Impact Engineering*, 95(7), 165–175. DOI 10.1016/j.ijimpeng.2016.05.003.
24. Rajeev, R., Rebecca, J. G., Yan, Z., Xing, M., Osama, Y. et al. (2020). A comprehensive review on the mechanical properties of waste tire rubber concrete. *Construction and Building Materials*, 237(10), 117651. DOI 10.1016/j.conbuildmat.2019.117651.
25. Yu, Z., Tang, R., Li, F., Hu, Y., Liu, G. et al. (2021). Experimental study and failure criterion analysis on combined compression-shear performance of rubber concrete (RC) with different rubber replacement ratio. *Construction and Building Materials*, 288(10), 123105. DOI 10.1016/j.conbuildmat.2021.123105.

26. Xu, J. H., Chen, S. L., Yu, H., Wang, Y. (2015). Crumb rubber concrete deterioration caused by sulphate attack. *Proceedings of the 3rd International Conference on Material, Mechanical and Manufacturing Engineering*, pp. 27–28. Guangzhou, China.
27. Xu, J. H., Feng, X. T., Chen, S. L., Shi, C. Y. (2012). Fundamental mechanical performances of rubber concrete. *Applied Mechanics and Materials*, 193, 1401–1404. DOI 10.4028/www.scientific.net/AMM.193-194.1401.
28. Huang, X., Wang, T., Pang, J., Song, F. (2021). Experimental study on the effect of freeze-thaw cycles on the apparent and mechanical properties of rubber concrete under chloride environment. *Arabian Journal for Science and Engineering*, 47(4), 4133–4153. DOI 10.1007/s13369-021-05922-y.
29. Molina-Gómez, F., Bulla-Cruz, L. A., Darghan, C. A. E. (2021). A novel approach for the control of grain size distributions based on variance analysis. *Construction and Building Materials*, 285(8), 122748. DOI 10.1016/j.conbuildmat.2021.122748.
30. Jnyanendra, K. P., Bulu, P. (2020). Multi-response optimization using Taguchi-Grey relational analysis for composition of fly ash-ground granulated blast furnace slag based geopolymer concrete. *Construction and Building Materials*, 241(32), 118049. DOI 10.1016/j.conbuildmat.2020.118049.
31. Chen, H. L., Li, D. D., Ma, X., Zhong, Z., El-Sayed, A. (2021). Mesoscale analysis of rubber particle effect on young's modulus and creep behaviour of crumb rubber concrete. *International Journal of Mechanics and Materials in Design*, 17(3), 659–678. DOI 10.1007/s10999-021-09552-y.
32. Wang, Z., Fu, J., Manes, A. (2021). Discrete fracture and size effect of aluminosilicate glass under flexural loading: Monte Carlo simulations and experimental validation. *Theoretical and Applied Fracture Mechanics*, 111, 102864. DOI 10.1016/j.tafmec.2020.102864.
33. Hillerborg, A., Modéer, M., Petersson, P. E. (1976). Analysis of crack formation and crack growth in concrete by means of fracture mechanics and finite elements. *Cement and Concrete Research*, 6(6), 773–781. DOI 10.1016/0008-8846(76)90007-7.
34. Peng, Y. J., Chen, Y., Wang, Q., Ying, L. P. (2020). Mesoscopic numerical simulation of fracture process and failure mechanism of cement mortar. *Structural Concrete*, 22, 831–842.
35. Peng, Y. J., Chen, X. Y., Ying, L. P., Chen, Y., Zhang, L. J. (2019). Mesoscopic numerical simulation of fracture process and failure mechanism of concrete based on convex aggregate model. *Advances in Materials Science and Engineering*, 2019, 5234327.
36. Wang, B., Zhu, E., Zhang, Z. (2022). Microscale fracture damage analysis of lightweight aggregate concrete under tension and compression based on cohesive zone model. *Journal of Engineering Mechanics*, 148(2), 211–220. DOI 10.1061/(ASCE)EM.1943-7889.0002051.
37. Sabbagh, Y. S. R., Amiri, T. (2021). An efficient automatic adaptive algorithm for cohesive crack propagation modeling of concrete structures using matrix-free unstructured galerkin finite volume method. *Computers and Mathematics with Applications*, 97(6), 237–250. DOI 10.1016/j.camwa.2021.06.004.
38. Naotunna, C. N., Samarakoon, S. M. S. M., Fosså, K. T. (2021). A new crack spacing model for reinforced concrete specimens with multiple bars subjected to axial tension using 3D nonlinear FEM simulations. *Structural Concrete*, 22(6), 3241–3254. DOI 10.1002/suco.202100025.
39. Javanmardi, M. R., Mahmoud, R. M., Mahmoud, R. M. (2019). Extended finite element method and anisotropic damage plasticity for modelling crack propagation in concrete. *Finite Elements in Analysis & Design*, 165(2), 1–20. DOI 10.1016/j.finel.2019.07.004.
40. Liu, J., Zhang, X., Lv, G., Wang, K., Han, B. et al. (2021). Study on crack development of concrete lining with insufficient lining thickness based on CZM Method. *Materials*, 14(24), 7862. DOI 10.3390/ma14247862.
41. Adrian, F., Günter, A. R. (2020). Simulation of crack growth in reinforced concrete beams using extended finite element method. *Engineering Failure Analysis*, 116(4), 104698. DOI 10.1016/j.engfailanal.2020.104698.
42. Kyoungsoo, P., Glaucio, H. P., Jeffery, R. R. (2008). Determination of the kink point in the bilinear softening model for concrete. *Engineering Fracture Mechanics*, 75(13), 3806–3818. DOI 10.1016/j.engfracmech.2008.02.002.
43. Turatsinze, A., Garros, M. (2008). On the modulus of elasticity and strain capacity of self-compacting concrete incorporating rubber aggregates. *Resources, Conservation and Recycling*, 52(10), 1209–1215. DOI 10.1016/j.resconrec.2008.06.012.

44. Savas, B. Z., Ahmad, S., Fedroff, D. (1996). Freeze-thaw durability of concrete with ground waste tire rubber. *Transportation Research Record*, 157(5), 80–88.
45. Hua, L. X., Xiao, F. P., Li, Y. T., Huang, H. B., Zhao, K. W. et al. (2020). A potential damage mechanism of rubberized cement under freeze-thaw cycle. *Construction and Building Materials*, 252, 119054. DOI 10.1016/j.conbuildmat.2020.119054.
46. Yao, W., Liu, Y., Wang, T., Pang, J. (2021). Performance degradation and microscopic structure of rubber/concrete after salt freeze-thaw cycles. *Fuhe Cailiao Xuebao/Acta Materiae Compositae Sinica*, 38(12), 4294–4304.